Journal of Glaciology



Article

Cite this article: Sartore NB, Haseloff M and Wagner TJW (2026) Feedbacks between ice shelf geometry and basal melt in plume parameterizations. *Journal of Glaciology* **72**, e79, 1–12. https://doi.org/10.1017/jog.2026.10189

Received: 22 January 2026 UTC
Revised: 8 June 2026 UTC
Accepted: 7 July 2026 UTC

Keywords:
ice/ocean interactions; ice shelves; melt - basal

Corresponding author:
Nicolas B. Sartore;
Email: nsartore@wisc.edu

© The Author(s), 2026. Published by Cambridge University Press on behalf of International Glaciological Society. This is an Open Access article, distributed under the terms of the Creative Commons Attribution licence (http://creativecommons.org/licenses/by/4.0), which permits unrestricted re-use, distribution and reproduction, provided the original article is properly cited.

Feedbacks between ice shelf geometry and basal melt in plume parameterizations

Nicolas B. Sartore[1], Marianne Haseloff[1,2] and Till J. W. Wagner[1]

[1]Atmospheric & Oceanic Sciences, University of Wisconsin-Madison, USA and [2]Geoscience, University of Wisconsin-Madison, USA

Abstract

Basal melting is a major component of Antarctic ice mass loss. It is mainly driven by the circulation of water in ice shelf cavities. One approximation of this circulation is by models of buoyant plumes rising along the ice shelf base. For large-scale ice sheet models, a local melt parameterization of plume models that can be applied at an ice shelf-wide scale is desirable, and such a parameterization has recently been proposed and shown to perform well compared to a spatially resolved plume model when the ice shelf profile is fixed. In this study, we test the local parameterization for a dynamically evolving ice shelf, which allows for feedbacks between basal slope and melt rate. We find that these feedbacks enhance melt for steep basal slopes and reduce melt for small slopes. This decreases the parameterization performance, and under certain conditions the parameterization introduces an unphysical melt discontinuity. This can lead to large differences in the predicted melt rate and ice shelf length compared to the nonlocal plume model. More generally, our findings suggest that i) local parameterizations should be applied with caution in coupled ice–ocean frameworks, and ii) melt parameterizations should be evaluated in coupled settings to avoid unwanted behavior.

1. Introduction

Basal melt accounts for approximately 50% of mass loss from Antarctic ice shelves (Rignot and others, 2013; Greene and others, 2022). It is expected to intensify due to the intrusion of warm water into sub-ice shelf cavities as a consequence of continued global warming (Jordan and others, 2023). Thus, an accurate representation of sub-shelf melt in models is essential to estimate ice shelf mass balance and the evolution of the Antarctic Ice Sheet (De Rydt and Naughten, 2024; Coulon and others, 2024b; Burgard and others, 2025).

Intricate ocean–ice geometries, complex physical processes and high computational costs make it challenging to resolve ocean conditions and dynamics in ice shelf cavities (Goldberg and others, 2019). This has hindered direct coupling efforts between climate and ice sheet models (Felikson and others, 2025). Parameterizing the basal melt rate as a function of ocean and ice shelf properties may provide a practical alternative for the next generation of modeling efforts. Short of dynamic coupling (be it direct or parameterized), melt parameterizations can be implemented in stand-alone ice sheet models, using oceanic conditions derived from climate model outputs as forcings (e.g., Favier and others, 2014; DeConto and Pollard, 2016; Lazeroms and others, 2018; 2019; Reese and others, 2018). However, no standardized and broadly accepted parameterization for ice shelf basal melt exists to date (Burgard and others, 2022).

The buoyancy-driven circulation of freshwater plumes rising along the ceiling of the cavity is understood to be responsible for a large part of basal melt (MacAyeal, 1985; Joughin and others, 2012; Straneo and Heimbach, 2013; Hewitt, 2020). Jenkins (2011) showed that a one-dimensional system, represented by four differential equations based on the physics of turbulent gravity currents, can effectively describe this circulation.

Despite its relative simplicity compared to a full cavity simulation, this parameterization remains impractical for large-scale ice sheet models and global climate models. A significant challenge lies in extending the one-dimensional plume model of Jenkins (2011) to two dimensions (e.g., Holland and others, 2007; Payne and others, 2007). Difficulties include incorporating the Coriolis term within the plume dynamics and addressing the substantial scale disparity between the plume width and the model resolution (e.g., Hewitt, 2020; Lambert and others, 2023). As an alternative, Lazeroms and others (2018) proposed a local simplification of the plume system using an 11-term polynomial fit. While performing well, this parameterization is cumbersome to use and prevents physical insight. Building on this earlier work, Lazeroms and others (2019) proposed a further local simplification derived in the limit of small basal slopes and small freshwater flux at the grounding line. The authors tested this parameterization for a

Downloaded from https://www.cambridge.org/core. 14 Nov 2026 at 21:14:43, subject to the Cambridge Core terms of use.

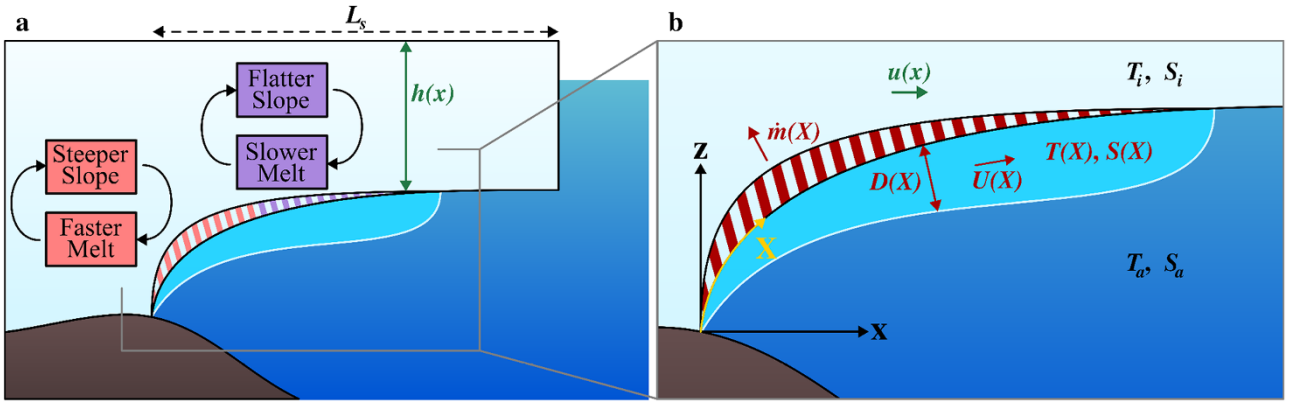


Figure 1. Diagram of an ice shelf cavity with plume. Panel a illustrates the feedbacks that result from the direct coupling between the ice shelf geometry and plume-induced melting. Here, $h(x)$ and L_s are the ice shelf thickness and length. Panel b is a zoom-in on the plume region and shows the plume thickness $D(X)$, velocity $U(X)$, temperature $T(X)$ and salinity $S(X)$. Note the difference between the horizontal coordinate x and the curvilinear coordinate X (yellow), which follows the ice–ocean interface and evolves with time. The directions of ice and plume flow, and melt rate $\dot{m}(X)$ are illustrated with arrows. Also indicated are the ice shelf temperature T_i and salinity S_i, as well as the ambient ocean temperature T_a and salinity S_a.

range of fixed ice shelf profiles. In this framework, the parameterization yields a close agreement with the 4-equation plume model of Jenkins (2011), with small tendencies to overestimate the melt near the grounding line and underestimate it further away.

Here, we compare the performance of the local parameterization of Lazeroms and others (2019) with the plume model of Jenkins (2011) in a framework where the plumes are coupled to a dynamically evolving ice shelf, i.e., under conditions where the ice geometry is no longer assumed fixed but flows and responds to the intensity of the local melt rate. Since the ice shelf geometry evolves as a function of the melt rate, the changing shape of the ice shelf, in turn, modifies the melt rate itself. Specifically, the plume-induced melt rate is sensitive to the basal slope and the ice shelf draft, which leads to a positive feedback between basal melt and ice shelf geometry, as illustrated in Fig. 1a: large melting steepens the basal slope, which further enhances melting. Conversely, a lower melt rate results in a shallower slope, reducing the overall melt intensity. Our findings demonstrate that these feedbacks exacerbate the error between the local parameterization and the full plume system. Moreover, the use of the local parameterization leads to unrealistic discontinuities in the melt rate for a range of conditions.

The details of the model implementation are provided in Section 2, while readers primarily interested in the results may proceed directly to Section 3. Finally, in Section 4, we discuss the potential implications of our findings, as well as the broader applicability and limitations of the coupled model introduced here.

2. Model setup

2.1. Ice flow and geometry

We consider a confined ice shelf flowing in the positive x—direction from the grounding line at $x = 0$ to the terminus at x_t. The ice flow is modeled using the Shallow Shelf Approximation (SSA), which is widely employed to simulate ice shelf dynamics (e.g., MacAyeal, 1989; Dupont and Alley, 2005; Nick and others, 2009; Hindmarsh, 2012; Pegler, 2016; Haseloff and Sergienko, 2018; 2022):

$$\frac{\partial}{\partial x}\left(\frac{h}{A^{1/n}}\left|\frac{\partial u}{\partial x}\right|^{\frac{1}{n}-1}\frac{\partial u}{\partial x}\right) - \frac{C_W A^{-\frac{1}{n}}}{W^{\frac{1}{n}+1}} h\,|u|^{\frac{1}{n}-1}\,u = \frac{1}{2}\rho_i g\left(1-\frac{\rho_i}{\rho_w}\right)h\frac{\partial h}{\partial x}, \tag{1}$$

with h the ice thickness, u the ice speed, A the ice viscosity rate factor, n the flow law exponent, ρ_i the ice density, ρ_w the seawater density, g the acceleration due to gravity, W the ice shelf width and C_W a lateral shear stress parameter. Parameter values are given in Table A1 (Appendix A). The ice thickness evolution is determined from mass conservation:

$$\frac{\partial h}{\partial t} + \frac{\partial}{\partial x}(uh) = -\dot{m}, \tag{2}$$

with $\dot{m}$ the melt rate (positive for melting; negative for freeze-on).

At the grounding line, ice flux and ice thickness are prescribed:

$$uh = q^{gl} \quad \text{and} \quad h = h^{gl} \quad \text{at } x = 0, \tag{3}$$

where the superscript 'gl' signifies 'grounding line'.

Stress balance is prescribed at the terminus, assuming a floating vertical ice front:

$$\frac{2}{A^{1/n}}h\left|\frac{\partial u}{\partial x}\right|^{\frac{1}{n}-1}\frac{\partial u}{\partial x} = \frac{1}{2}\rho_i g\left(1-\frac{\rho_i}{\rho_w}\right)h^2 \quad \text{at } x = x_t. \tag{4}$$

The position of the terminus, x_t, is determined by the melt rate: for low to moderate melt rates, it is fixed at $x_t = L_s$, but for sufficiently strong melt, the ice thickness can go to zero at $x_t < L_s$. The terminus position is indirectly determined as the first location where $h = 0$:

$$\begin{cases} x_t = L_s & \text{if } h > 0 \,\forall\, x, \\ h(x_t) = 0 & \text{otherwise.} \end{cases} \tag{5}$$

2.2. Buoyant meltwater plume model

We assume that a buoyant meltwater plume drives circulation in the ice shelf cavity (illustrated in Fig. 1b), which sets the sub-shelf melt rate (Jenkins, 1991; 2011; Hewitt, 2020). In this case, the basal melt rate is determined by the thermohaline difference between freshwater released from subglacial discharge and melted ice on the one hand and saline ocean water underneath the ice shelf on

Downloaded from https://www.cambridge.org/core. 14 Nov 2026 at 21:14:43, subject to the Cambridge Core terms of use.

the other hand (Jenkins, 2011). Generally, this leads to high melt rates close to the grounding line and possible refreezing further away. As discussed above, we compare two specific representations of this general plume model (Jenkins, 2011; Lazeroms and others, 2019):

2.2.1. Full plume model

We refer to the one-dimensional buoyancy-driven plume model from Jenkins (2011) as the 'full plume model'. The model is described by conservation of mass (6a), momentum (6b), buoyancy (6c) and sensible heat (6d) within the plume:

$$\frac{\partial}{\partial X}(DU) = \sin\alpha\, E_0 U + \dot{m}, \tag{6a}$$

$$\frac{\partial}{\partial X}(DU^2) = \sin\alpha\, gD\Delta\rho - C_d U^2, \tag{6b}$$

$$\frac{\partial}{\partial X}(DU\Delta\rho) = \sin\alpha\, \frac{d\Delta\rho_a}{dz_b} DU + \dot{m}\Delta\rho_i^{ef}, \tag{6c}$$

$$\frac{\partial}{\partial X}(DU\Delta T) = \sin\alpha\, \left(T_a - T_{af}\right) E_0 U + \left(T_i^{ef} - T_{if}\right)\dot{m} - \sin\alpha\, \lambda_3 DU. \tag{6d}$$

Here,

$$X = \int_0^x \sqrt{1 + \left(\frac{\rho_i}{\rho_w}\frac{\partial h}{\partial x}\right)^2}\, \mathrm{d}x \tag{7}$$

is the curvilinear coordinate along the shelf base, D the plume thickness, U the plume velocity, S the plume salinity and T the plume temperature. The density difference between plume and ambient ocean is given by $\Delta\rho = \beta_S(S_a - S) - \beta_T(T_a - T)$, with S_a and T_a the ambient ocean salinity and temperature, and β_S and β_T the haline contraction and thermal expansion coefficients. $\Delta T = T - T_f$ is the temperature of the plume relative to its freezing temperature T_f. The ice shelf is in isostatic equilibrium, with the draft $z_b(x) = -h(x)\rho_i/\rho_w$. The local basal slope is

$$\sin\alpha = -\frac{\partial h/\partial x}{\sqrt{(\rho_w/\rho_i)^2 + |\partial h/\partial x|^2}}. \tag{8}$$

Furthermore, in Equation (6d), E_0 is the plume entrainment coefficient, C_d the drag coefficient, $d\Delta\rho_a/dz_b$ the slope of the ambient density contrast, $\Delta\rho_i^{ef}$ is the effective meltwater density contrast, T_{af} is the ambient water freezing temperature, T_{if} is the meltwater freezing temperature and T_i^{ef} is the effective meltwater temperature (see Table A2 in Appendix A for expressions and parameter values).

The melt rate induced by the plume on the ice shelf $\dot{m}$ is assumed to be directly proportional to the thermal forcing ΔT and the plume velocity U, such that

$$\dot{m} = M_0 U \Delta T, \tag{9}$$

where M_0 is the melt rate factor (in $^\circ\mathrm{C}^{-1}$, see Table A2 in Appendix A).

At the grounding line, the plume is initiated by subglacial discharge. This discharge is assumed to be freshwater at freezing temperature, such that the initial conditions for the plume water are $S^{gl} = 0$ psu and $T^{gl} = T_f^{gl}$. From this we determine $\Delta\rho^{gl} = \beta_S S_a - \beta_T\left(T_a - T_f^{gl}\right)$ and $\Delta T^{gl} = T^{gl} - T_f^{gl} = 0$. The local plume representation defined below assumes no freshwater flux at the grounding line. For numerical stability, we introduce a small initial freshwater flux $DU^{gl} = 10^{-6}\ \mathrm{m^2 s^{-1}}$ for full plume simulations. The plume thickness at the grounding line is arbitrarily set to $D^{gl} = 1$ m. Varying D^{gl} over three orders of magnitude indicates negligible impacts on the results (see Fig. B2 in Appendix B).

2.2.2. Local plume model

Lazeroms and others (2019) present a local approximation of plume-induced melting for constant and small basal slopes, based on asymptotic expansion and order of magnitude comparison. We will refer to this parameterization as the 'local plume model'. In this model, the melt rate is determined from

$$\dot{m} = \left(T_a - T_f^{gl}\right)^2 \mathcal{M}(\bar{x}) \sqrt{\frac{\beta_S S_a g c^3}{\lambda_3 L^3}} \times \sqrt{\frac{1 - c_{\rho 1}\Gamma}{C_d + E_0\sin\alpha}} \left(\frac{\Gamma E_0 \sin\alpha}{\Gamma + c_\tau + E_0\sin\alpha}\right)^{3/2}, \tag{10a}$$

where $\mathcal{M}(\zeta)$ is a non-dimensional melt function that varies with distance from the grounding line:

$$\mathcal{M}(\zeta) = 2^{-3/2}\left[3(1-\zeta)^{4/3} - 1\right]\sqrt{1 - (1-\zeta)^{4/3}}. \tag{10b}$$

In Equation (10a), $\bar{x}$ is the non-dimensional vertical distance from the grounding line depth with a slope-dependent correction factor:

$$\bar{x} = \lambda_3 \frac{z_b - z_b^{gl}}{T_a - T_f^{gl}} \left[1 + C_\epsilon \left(\frac{E_0\sin\alpha}{\Gamma + c_\tau + E_0\sin\alpha}\right)^{\frac{3}{4}}\right]^{-1} \tag{10c}$$

Other constants are defined in Tables A1 and A2 in Appendix A.

Formally, the derivation of the local plume model assumes small, uniform basal slopes and uniform ocean conditions. However, it was found to compare well to the full plume model even when allowing for non-uniform basal slope and ocean conditions (Lazeroms and others, 2019).

The steady-state ice shelf model (1)–(2) coupled either to the full plume (6a)–(9) or the local plume (10a)–(10c) can be reformulated as systems of first-order ordinary differential equations and are solved using the Python package SciPy's integrate.solve_ivp (Virtanen and others, 2020). The time-dependent system is solved with a finite-difference discretization using PETSc (Balay and others, 2026). The steady-state solutions are compared to converged solutions of the PETSc integration in Fig. B1 for verification of the numerical methods (Appendix B).

3. Results

3.1. Plume model evaluation

Our results indicate that for a range of conditions, the local plume model leads to unphysical behavior once it is coupled to an evolving ice shelf. Fig. 2a shows a representative solution for a steady-state ice shelf with Thwaites Ice Shelf-like conditions: the grounding line thickness is $h^{gl} = 800$ m, the initial ice velocity is $u^{gl} = 2000\ \mathrm{m\,a^{-1}}$, the width of the shelf is $W = 80$ km and the ambient ocean temperature T_a depends on the depth and is extracted from Burgard and others (2022) (see Appendix C for details). In this scenario, the melt rate shows a discontinuity (or jump) to $\dot{m} = 0$ at $x_d = 10.5$ km. This leads to a uniform ice thickness $h\,(x > x_d)$ and beyond that

Downloaded from https://www.cambridge.org/core. 14 Nov 2026 at 21:14:43, subject to the Cambridge Core terms of use.

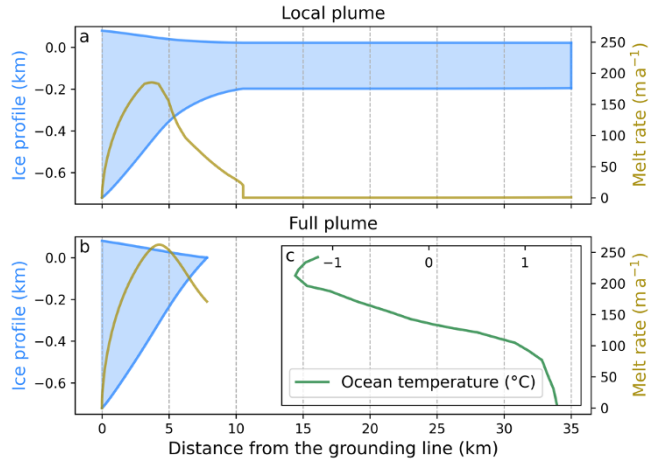


Figure 2. Ice profiles (blue) and melt rates (olive) for the steady-state solution of the coupled ice shelf–melt model with buttressing, for the local plume model in panel a and the full plume model in panel b. Here, ocean temperature is depth-varying (data from Burgard and others (2022); shown in inset c, which has the same vertical axis as the main panel). See text for other simulation parameters and Appendix C for details on the temperature profile.

point the melt is zero or small (but always positive). Conversely, the full plume (6a)–(9) leads to ice shelf melting and thinning until it reaches zero thickness at $x_t = 7.8$ km (Fig. 2b).

Figure 2 illustrates the discontinuity in a simulation that includes buttressing effects, in addition to the variable ocean temperature profile. As we discuss below in Section 4, buttressing and ocean temperature variations do not cause the melt discontinuity. We therefore neglect buttressing (by formally assuming $W \to \infty$ in Eq. (1)) and assume a uniform ocean temperature from here on.

To confirm that the results shown in Fig. 2 are not due to a numerical instability or the assumption of steady-state, we consider the time-dependent system (solved using PETSc). The initial state is obtained from a prior simulation of the coupled full plume model run to steady-state at an ocean temperature of $T_a = -1.9°C$. Both the full plume PETSc simulation and the local plume PETSc simulation are initialized with this ice shelf (Fig. 3a and b, respectively). The ocean temperature is increased to $T_a = -1.6°C$ and the model is integrated to a new steady state for both the full plume (left column of Fig. 3) and the local plume (right column). For the local plume model, a small perturbation in the otherwise smooth melt emerges at the grounding line and propagates downshelf shortly after initialization (see $x = 4$ km in Fig. 3d). The perturbation continues to propagate and grow, and a discontinuity appears at $x = 6$ km as shown in Fig. 3f. The discontinuity then sharpens and propagates until it becomes stationary at $x = 8$ km (Fig. 3h). This unphysical behavior is known as a shock (e.g., Fowler, 1997). Conversely, in the full plume model, melt is continuous along the full extent of the ice shelf and the ice shelf front melts completely by the end of the simulation, with the front retreating to $x_t = 19$ km (Fig. 3g).

3.2. Origin of the melt discontinuity

The highly nonlinear dependence of the melt rate on ice shelf slope $\sin\alpha$ and thickness h prevents a closed-form analytical solution, but we can qualitatively understand the problematic behavior. Momentarily neglecting the slope-dependent correction factor in Equation (10c), the local plume melt rate depends on basal slope as:

$$\dot{m} \propto \sqrt{\frac{1 - c_{\rho 1}\Gamma}{C_d + E_0 \sin\alpha}} \left(\frac{\Gamma E_0 \sin\alpha}{\Gamma + c_\tau + E_0 \sin\alpha} \right)^{3/2}. \tag{11}$$

The qualitative behavior is shown in Fig. 4a (olive line).

Importantly, $\dot{m} \to 0$ for $\sin\alpha \propto \partial h/\partial x \to 0$. To see why this is problematic, we can integrate the momentum balance Equation (1) with $W \to \infty$ by use of the boundary condition at the calving front (4) to obtain (e.g., Schoof, 2007)

$$\frac{h}{A^{1/n}} \left| \frac{\partial u}{\partial x} \right|^{\frac{1}{n}-1} \frac{\partial u}{\partial x} = \rho_i g \left(1 - \frac{\rho_i}{\rho_w}\right) h^2. \tag{12}$$

Introducing the flux $q = uh$ and rearranging gives

$$\frac{1}{h}\frac{\partial q}{\partial x} - \frac{q}{h^2}\frac{\partial h}{\partial x} = A \left[\rho_i g \left(1 - \frac{\rho_i}{\rho_w}\right)\right]^n h^n, \tag{13a}$$

$$\frac{\partial q}{\partial x} = \dot{m}, \tag{13b}$$

with the last equation the steady-state version of (2). The discontinuity occurs mid-shelf at finite ice thicknesses, that is $h > 0$. Assuming this is the case, we can see that in the limit of $\partial h/\partial x = 0$, the first Equation (13a) requires $h = 0$ for $\partial h/\partial x = \partial q/\partial x = 0$ when $\dot{m}(\partial h/\partial x = 0) = 0$. Since $h > 0$ and $h = 0$ cannot be satisfied simultaneously, unphysical behavior ensues. Physically, this means that when the ice thickness and flux simultaneously become constant, mass balance requires the velocity to be constant too (as $q = uh$). However, the momentum balance requires the velocity to linearly increase for constant, non-zero ice thicknesses in order to satisfy the force balance at the calving front. This latter behavior can be seen in the velocity solutions past the discontinuity (not shown).

The earlier 11-term plume parameterization by Lazeroms and others (2018) prescribes the same dependence on ice shelf slope and consequently shows the same discontinuity (see Fig. B3 in Appendix B and Discussion). Conversely, in the full plume model a zero slope does not automatically require $\dot{m} \to 0$, and the problem does not arise.

3.3. Regularization of the melt discontinuity

We can further show that the problematic behavior is linked to the limiting behavior of $\dot{m}(\partial h/\partial x \to 0)$ by regularizing the melt rate so that $\dot{m}(\partial h/\partial x \to 0) \neq 0$. The simplest such regularization replaces the slope used in the melt equation so that it does not fall below a prescribed threshold:

$$\sin\alpha' = \max\left(\sin\alpha,\ \sin\alpha_c\right). \tag{14}$$

Here, we choose the threshold $\sin\alpha_c$ that maximizes the melt rate $\dot{m}$ for small slopes. This can be determined analytically from Equation (10a) when the slope-dependent correction factor is neglected:

$$\sin\alpha_c = \frac{\Gamma + c_\tau}{E_0} \left(1 + \sqrt{1 + 3\frac{C_d}{\Gamma + c_\tau}}\right). \tag{15}$$

This simple regularization effectively prevents the discontinuity described above (Fig. 4b) without significantly affecting other parameter ranges (not shown). By limiting the slope within the melt function, the late-stage behavior of the plume

Downloaded from https://www.cambridge.org/core. 14 Nov 2026 at 21:14:43, subject to the Cambridge Core terms of use.

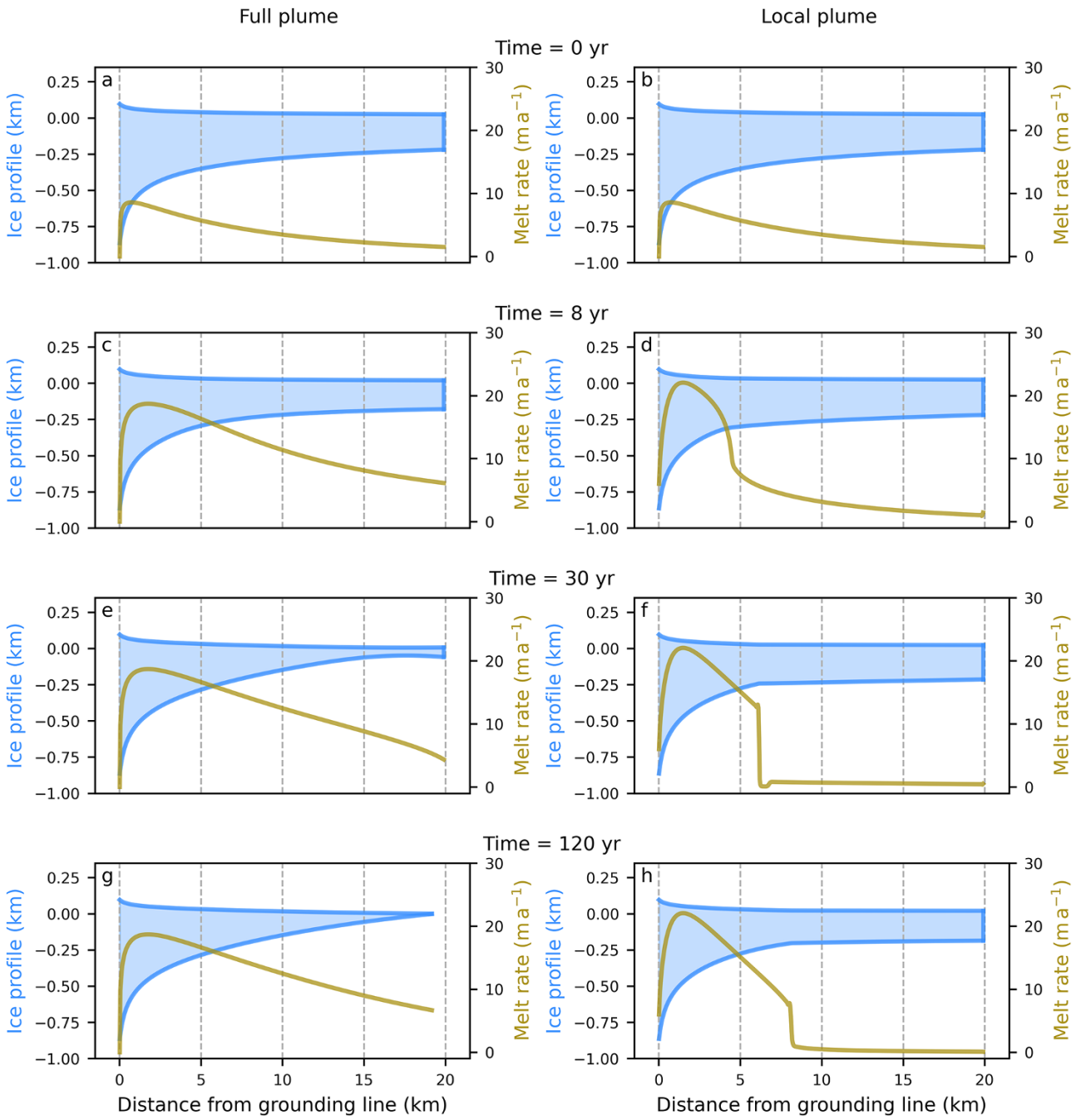


Figure 3. Snapshots of the time-dependent solution of the coupled ice shelf–melt model. The ice shelf profiles (blue) and melt rates (olive) are shown for both the full plume model (left column) and the local plume model (right column). Solutions are shown at $t = 0$, 8, 30 and 120 years. The grounding line thickness is $h^{gl} = 1000$ m, the initial ice velocity is $u^{gl} = 250$ m a^{-1} and the ambient ocean temperature is $T_a = -1.6°$C. The initial state in panels a and b is given by the steady-state solution of the coupled full plume model with an ocean temperature $T_a = -1.9°$C.

(melt/refreezing) is preserved in most cases, while the sudden melt discontinuity is avoided (Fig. 4a).

3.4. Plume parameterization impact on melting

To identify the range of solutions that feature the unphysical behavior described above, we compare steady-state solutions of the full plume model to those of the local plume model over a wide range of parameters. We focus on varying the grounding line thickness (h^{gl}) and the uniform ambient ocean temperature (T_a). Here, we consider the dependence of two ice shelf properties on these parameters: ice shelf length L_s (top row in Fig. 5) and mean melt rate (bottom row in Fig. 5)—which can be estimated from the ice flux difference as: $\frac{1}{x_t}\int_0^{x_t} \dot{m}dx = \left[q^{gl} - q\left(x_t\right)\right]/x_t$.

The hatched regions in Fig. 5b and e delineate areas where discontinuities in the melt rate occur. These discontinuities appear in two distinct branches, corresponding to the two melt–slope feedback mechanisms illustrated in Fig. 1a. The melt–slope feedbacks are a physical feature of the system and act in both the full

Downloaded from https://www.cambridge.org/core. 14 Nov 2026 at 21:14:43, subject to the Cambridge Core terms of use.

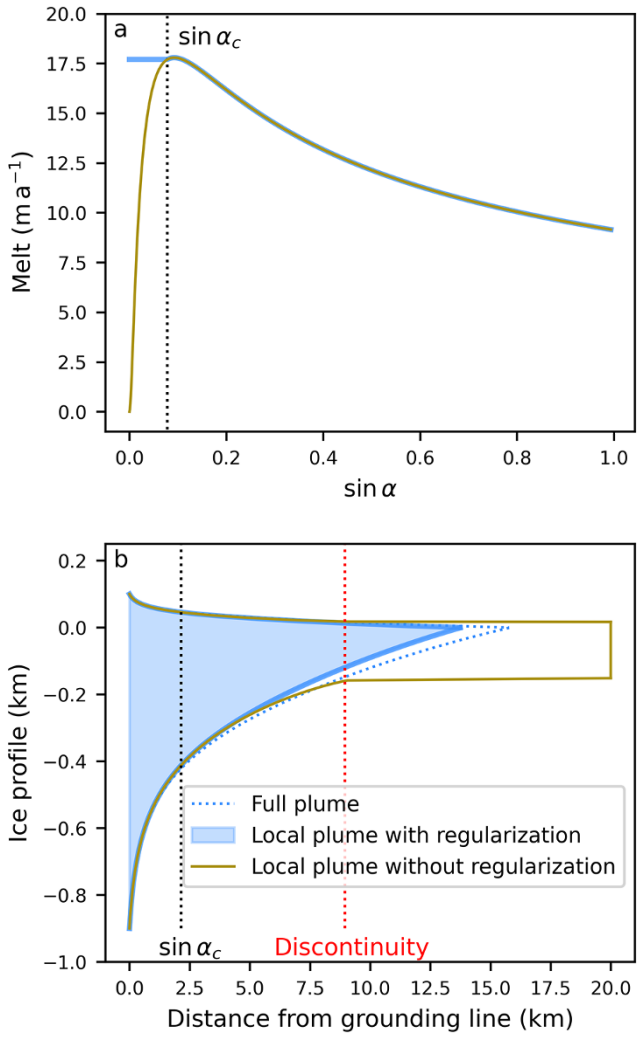


Figure 4. Example of the regularized melt (solid blue) compared to the default local plume parameterization (olive). Panel a illustrates the melt rate as a function of the slope ($\sin\alpha$) at the location of the discontinuity (dotted red line in panel b), while panel b shows the ice thickness profile with the full plume solution in dotted blue.

and local plume models. However, the feedbacks only manifest as discontinuities in the local plume model.

The roughly vertical branch, occurring at temperatures between -1.6°C and -1.1°C, corresponds to the instability discussed above due to a feedback of shallower slopes leading to less melt and less viscous thinning. In this regime, the discrepancies between the local and full plume models are substantial: the ice-shelf length is overestimated by up to approximately 9 km (90 % relative error), and the mean melt rate is underestimated by up to 20 m a^{-1} (50 % relative error).

The horizontal branch, characterized by initial ice thicknesses ranging from 80 to 150 m and exhibiting little sensitivity to ocean temperature, originates from this feedback operating in reverse with steeper slopes leading to more melt. In this parameter regime, the feedback induces rapid thinning at the ice front (not shown). This positive feedback was previously identified in a coupled modeling framework by Haseloff and Sergienko (2022), using a simplified plume parameterization. Our results suggest that this behavior is not an artifact of their simplified framework but rather a physical process and an intrinsic feature of plume-based parameterizations in the limit of steep slopes, which can emerge under realistic ice-shelf conditions. For the full plume model, the steep-slope feedback also results in an abruptly terminating ice shelf, but without introducing a discontinuity in the melt rate. Relative to the full plume model, the length differs by ± 2 km (up to 30 % relative error) and the mean melt rate is up to 6 m a^{-1} less (30 % relative error).

For the remainder of this study, we focus on the shallow-slope feedback regime, since despite inducing some discrepancies in the predicted melt rates and ice-shelf length, the overall physical behavior remains consistent between the local and full plume models in the steep-slope regime.

Outside of the discontinuity regimes, we find that in the coupled system, the local plume introduces errors of up to $\pm$ 2 km (30 % relative error) in the predicted shelf length (Fig. 5c). The average melt rates differ by up to $\pm$ 20 m a^{-1} depending on the conditions, which corresponds to a relative error of 20 to 30 %. For cold ocean temperatures (< -1.8°C), the relative error between the full and local plume formulations can reach 80%. The error in melt is partially obscured when considering average melt rates, as the mean smooths out discrepancies between the two models. Specifically, the local plume tends to overestimate melt near the grounding line and underestimate it farther downstream, resulting in partial compensation of local melt-rate errors.

4. Discussion

The unphysical behavior of local plume parameterizations in a coupled setting has—to our knowledge—not been previously reported, even though the coupled setting has been used in several previous studies (Favier and others, 2019; Berends and others, 2023; Coulon and others, 2024a). We hypothesize that this omission is due to the subtle nature of the instability, which makes it hard to detect in models with complex ice shelf geometries and coarser resolution. Moreover, a continuously evolving grounding line, ice influx or oceanic conditions may mute its effects or prevent its emergence altogether.

The unphysical behavior of the local plume melt observed above arises from its coupling with ice dynamics. Near the grounding line, both the melt rate and the basal slope are large, and the local plume model performs relatively well compared to the full plume model. Further away from the grounding line, the ice shelf flattens because of viscous thinning, leading to a reduction in melt. Under cold ambient ocean temperatures (~ -1.9°C) and small basal slopes, the melt rate varies smoothly, resulting in a gradual transition to flatter ice shelves. However, the melt rate sensitivity to changes in basal slope—and hence the feedback between ice geometry and melt—increases with ambient ocean temperature. This leads to the abrupt decrease in slope and melt at relatively warmer temperatures (~ -1.5°C) in the local plume model. For a range of temperatures and grounding line thicknesses, this transition becomes so sharp that it manifests as a sudden discontinuity in both melt rate and slope. The finding that the polynomial parameterization from Lazeroms and others (2018), exhibits the same type of instability (cf. Fig. B3 in Appendix B) supports our conclusion that the instability results from the locality of the parameterization.

The nonlinear dependence of the melt rate on ice shelf slope $\sin\alpha$ and thickness h prevents a closed-form analytical solution of the model. However, we can qualitatively understand its emergence by considering the limit of $\partial h/\partial x \to 0$, as discussed in Section 3.2. In the local melt rate parameterizations, there is no melt at vanishing ice shelf slopes, requiring a constant ice shelf flux, and hence ice velocity in steady state. For non-zero ice thicknesses, this violates

Downloaded from https://www.cambridge.org/core. 14 Nov 2026 at 21:14:43, subject to the Cambridge Core terms of use.

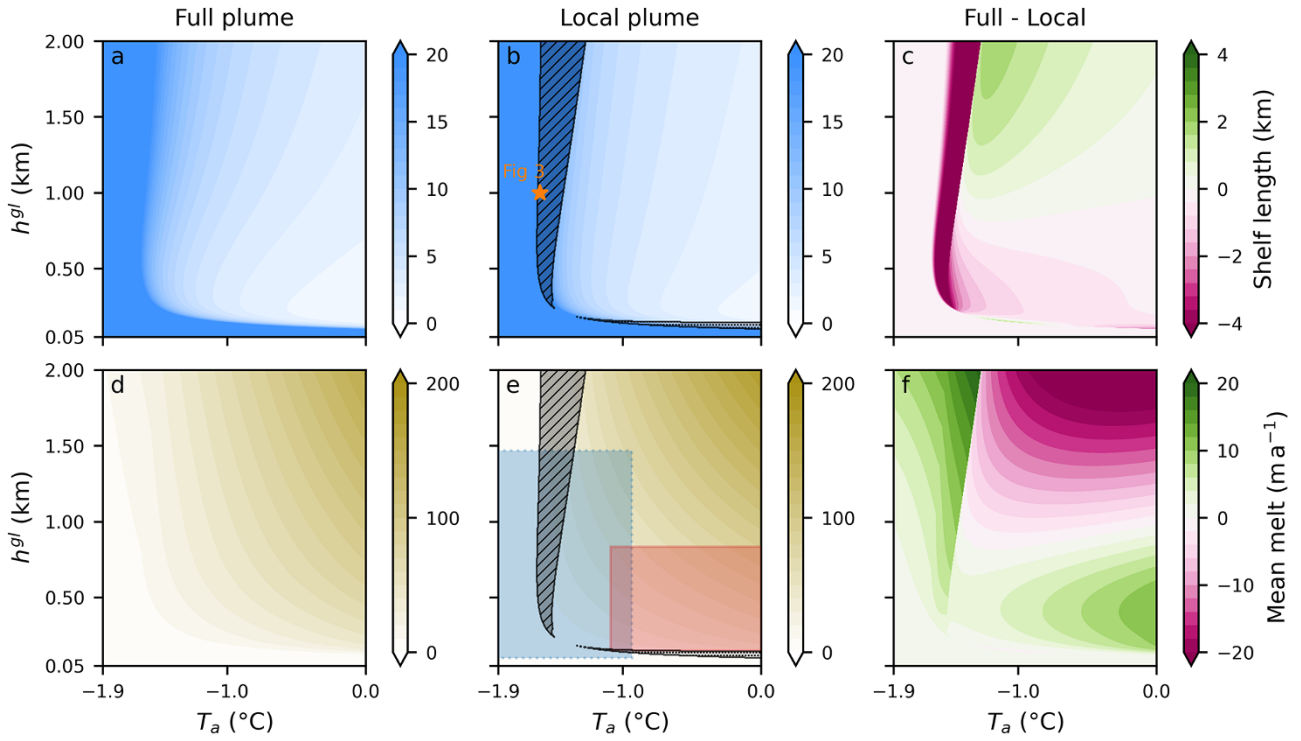


Figure 5. Sensitivity of the coupled model to changes in ambient ocean temperature T_a and initial ice thickness h^{gl}. Each simulation is performed for both the full plume model (left column) and the local plume model (middle column), with the difference shown in the right column. The first row shows contours of ice shelf length, and the second row shows contours of average melt rates. The hatched areas in panels b and e show regions of discontinuity in the melt rate. The two boxes in panel e broadly indicate the relevant parameter space for ice shelves around Antarctica: blue with dashed outline for cold cavities, and red with solid outline for warm cavities (Appendix C provides details on the calculation and data used for the box extents). The orange star in panel b marks the examples shown in Figure 3.

the momentum balance equation, which requires an increasing ice velocity in the downstream direction for constant ice thicknesses. Notably, the condition of vanishing melt at vanishing basal slope is present in both local formulations (Lazeroms and others, 2018; 2019), which explains why both parameterizations exhibit the same discontinuity behavior.

4.1. Relevance for realistic ice shelf studies

To assess the relevance of the instability for real ice shelves, we consider representative values for h^{gl} and T_a for both cold and warm ice shelves, which are indicated in Fig. 5e by the blue and red bounding boxes, respectively. To determine these ranges, we used the annual mean ocean temperature between 200 m below sea level and the sea bed in front of 18 Antarctic ice shelves from the World Ocean Atlas 2023 (Reagan and others, 2024). The grounding line thickness was estimated by averaging the ice thickness over a 4 km wide strip centered around the grounding line. We used the BedMap3 dataset for both ice thickness and grounding line position (Pritchard and others, 2025). The two temperature regimes were then identified based on the clustering of ocean temperature. The 'cold' regime comprises the Ross, Mertz, Totten, Shackleton, Amery, Filchner, Ronne, Larsen and Dotson ice shelves (blue box, $T_a \in [-1.9, -0.9]$°C), whereas the 'warm' regime includes the Rennick, Cook, Baudouin, Stancomb-Brunt, Wilkins, Abbot, Getz, Pine Island and Fimbul ice shelves (red box, $T_a \in [-1.1, 0.5]$°C). Further details regarding the classification method and the data used are provided in Appendix C. The 'cold' box largely contains the region of instability (hatched area), indicating that this issue is applicable to relevant ice shelf environments. Aside from the instability, the parameterization induces a relative melt rate error of -80% to 25% for cold ice shelves, depending on the initial condition. In contrast, the 'warm' box barely overlaps with the hatched area, but some of the warm shelves also encounter substantial melt bias (underestimations of 10%–30%), in particular since the boxes represent standard deviations around mean values, not the minimum/maximum values of h^{gl} and T_a.

4.2. Study limitations

The results presented above are derived from a highly idealized framework. This allows us to understand and evaluate the performance of different melt rate parameterizations, but we omit several processes that may limit the extension of our results to more complex conditions. The most substantial limitation of our study may be the use of a 1D-flowline model. Realistic ice shelf geometries are complex and deviate significantly from the channel flow assumed here. When considering two horizontal dimensions, the local plume parameterization would still require a vanishing steady-state flux divergence for flat ice shelves. However, it is not immediately obvious what the dynamic consequences of this requirement are. Our results in Fig. 2 illustrate that buttressing by itself is not sufficient to mitigate the melt discontinuity, and future work should investigate the consequences of the local parameterization to verify that it does not lead to unintended melt artifacts which might be obscured by the complexity of the problem.

The one-dimensional nature of the model also assumes alignment of plume and ice flow. In reality, this assumption is unlikely to hold: the plume trajectory is influenced by variations in basal topography, the Coriolis force deflects plumes over long distances,

Downloaded from https://www.cambridge.org/core. 14 Nov 2026 at 21:14:43, subject to the Cambridge Core terms of use.

and external forcings such as sub-shelf circulation and tides can significantly modify the plume path. Nevertheless, we consider our findings to remain relevant for two main reasons: i) The one-dimensional limitation is not unique to the local parameterization but is inherent to the original full plume model. Thus, the framework adopted here is consistent with the assumptions under which the local parameterization was originally derived, and a proper two-dimensional extension remains an important but separate future effort. ii) The local parameterization has been proposed (Lazeroms and others, 2019) as a two-dimensional melt parameterization applicable across ice-shelf cavities without explicit representation of the plume along flow paths. It is reasonable to expect that limitations identified in the one-dimensional setting provide a useful indicator of the potential issues in a two-dimensional context.

For the majority of this study, we neglected ocean temperature stratification. While important for a more realistic depiction of ice shelf dynamics, our results in Fig. 2 indicate that this simplification does not prevent the occurrence of the identified discontinuity.

We also assume that the ice is at a constant temperature of $T = 0°C$. In reality, ice shelves exhibit a temperature gradient, with a colder surface and a relatively warmer base, resulting in variations in ice stiffness. This influences both the melt rate and the plume's development through two primary mechanisms: (i) the impact on ice dynamics and (ii) the sensible heat required to warm the ice near the interface and bring it to the melting point. The latter has a minimal effect on melting and was shown to be negligible in the local plume parameterization by Lazeroms and others (2019). However, regarding (i), Sergienko and others (2013) showed that the changes in stiffness can induce important changes in geometry and thus melt, with differences up to 20% in the case of warm cavities.

The proposed regularization of the local plume model introduces only minor discrepancies with the full plume model in our non-buttressed, flow-line ice-shelf framework. However, real ice shelves experiencing significant buttressing typically exhibit smaller basal slopes at the grounding line than those predicted by our model. Consequently, the proposed regularization may not be appropriate for such ice shelves, as it would lead to an overestimation of melt rates. The regularization introduced here should be interpreted primarily as confirmation that the underlying issue has been correctly identified, rather than as a definitive correction of the local plume model.

The model employed here does not include a calving parameterization, which explains the unrealistic scenario of the shelf gradually reaching $h = 0$ at $x = x_t$. In reality, an ice shelf would likely calve once its thickness falls below a certain threshold or when some stress criterion is passed (e.g., van der Veen, 1998; Benn and others, 2007; Nick and others, 2010; Choi and others, 2021). However, the discussion in Section 3.2 is independent of the calving law, so that the behavior reported here remains relevant with the inclusion of a calving law, in particular when calving is not triggered before the melt discontinuity occurs.

Finally, it is worth noting that plume parameterizations are not the only viable approach for representing basal melting beneath ice shelves, with several studies having explored a range of avenues that could serve as an alternative to the local plume parameterization, in particular if the issues identified here prove significant in two dimensions (Reese and others, 2018; Favier and others, 2019; Burgard and others, 2022; Berends and others, 2023; Coulon and others, 2024a).

5. Conclusion

The gravity-driven circulation in ice shelf cavities is believed to be a key cause of basal melting. Yet, high complexity and computational cost prevent full cavity simulations in climate models for long timescales or for large ensembles. Standalone ice sheet models require melt parameterizations to incorporate ocean simulations and improve boundary representation (Levermann and others, 2020; Seroussi and others, 2020). Consequently, sub-shelf melt must be parameterized in both modeling frameworks. In this study, we explored one basal melt rate parameterization—proposed by Lazeroms and others (2019)—which simplifies the full plume parameterization from Jenkins (2011) to a local approximation. This parameterization has previously been validated for fixed ice shelf configurations only, i.e., without accounting for feedback between the computed melt rate and the evolving basal profile (e.g., Burgard and others, 2022). To assess the robustness of the local parameterization, we developed a dynamically coupled model that integrates ice shelf evolution and plume-induced melt rates. We report that under certain conditions of ambient ocean temperature and grounding line ice thickness, the local melt rate parameterization exhibits unphysical behavior as it does not allow mass and momentum balances to be satisfied simultaneously. This anomaly results in melt rate discontinuities and in the prediction of unphysically long and thick ice shelves.

The range of ambient ocean temperatures for which the discontinuity is observed is around $-1.6°C$ to $-1.1°C$ for grounding line ice thicknesses larger than $\sim$ 200 m, which is in the range found near a number of Antarctic ice shelves. Outside this parameter space, the coupling induces greater discrepancy than in a fixed model: the mean melt rate can show a difference of $\pm$ 20 m a^{-1} relative to the full plume model, with a tendency to underestimate melt rates in the parameter range relevant for Antarctic ice shelves. We conclude that unintended artifacts can arise when coupling ice sheet dynamics to melt processes. Future work should evaluate these effects and feedbacks of local melt rate parameterizations in a two-dimensional coupled framework.

Acknowledgements. N.B.S. and T.J.W.W. were supported by the NSF Office of Polar Programs through grants # 2148544 and # 2338057. M.H. acknowledges NSF grant # 2218463. This research was supported in part by grant NSF PHY-2309135 to the Kavli Institute for Theoretical Physics (KITP). Finally, we thank the reviewers for their thorough and thoughtful feedback.

References

Balay S and 35 others (2026) PETSc/TAO users manual. Technical Report ANL-21/39 - Revision 3.25, Argonne National Laboratory. doi: 10.2172/2998643.

Benn DI, Hulton NRJ and Mottram RH (2007) 'Calving laws', 'sliding laws' and the stability of tidewater glaciers. *Annals of Glaciology* **46**, 123–130.

Berends CJ, Stap LB and van de Wal RSW (2023) Strong impact of sub-shelf melt parameterisation on ice-sheet retreat in idealised and realistic Antarctic topography. *Journal of Glaciology* **69**(277), 1434–1448. doi: 10.1017/jog.2023.33.

Burgard C, Jourdain NC, Mosbeux C, Caillet J, Mathiot P and Kittel C (2025) Ocean warming threatens the viability of 60% of Antarctic ice shelves. *Nature* **647**(8088), 102–108. doi: 10.1038/s41586-025-09657-w.

Burgard C, Jourdain NC, Reese R, Jenkins A and Mathiot P (2022) An assessment of basal melt parameterisations for Antarctic ice shelves. *The Cryosphere* **16**(12), 4931–4975. doi: 10.5194/tc-16-4931-2022.

Choi Y, Morlighem M, Rignot E and Wood M (2021) Ice dynamics will remain a primary driver of Greenland ice sheet mass loss over the next century. *Communications Earth & Environment* **2**(1), 1–9. doi: 10.1038/s43247-021-00092-z.

Downloaded from https://www.cambridge.org/core. 14 Nov 2026 at 21:14:43, subject to the Cambridge Core terms of use.

Coulon V and 6 others (2024b) Disentangling the drivers of future Antarctic ice loss with a historically calibrated ice-sheet model. *The Cryosphere* **18**(2), 653–681. doi: 10.5194/tc-18-653-2024.

Coulon V, De Rydt J, Gregov T, Qin Q and Pattyn F (2024a) Future freshwater fluxes from the Antarctic ice sheet. *Geophysical Research Letters* **51**(23), e2024GL111250. doi: 10.1029/2024GL111250.

De Rydt J and Naughten K (2024) Geometric amplification and suppression of ice-shelf basal melt in West Antarctica. *The Cryosphere* **18**(4), 1863–1888. doi: 10.5194/tc-18-1863-2024.

DeConto RM and Pollard D (2016) Contribution of Antarctica to past and future sea-level rise. *Nature* **531**(7596), 591–597. doi: 10.1038/nature17145.

Dupont TK and Alley RB (2005) Assessment of the importance of ice-shelf buttressing to ice-sheet flow. *Geophysical Research Letters* **32**(4), 2004GL022024. doi: 10.1029/2004GL022024.

Favier L and 7 others (2019) Assessment of sub-shelf melting parameterisations using the ocean–ice-sheet coupled model NEMO(v3.6)–Elmer/Ice(v8.3). *Geoscientific Model Development* **12**(6), 2255–2283. doi: 10.5194/gmd-12-2255-2019.

Favier L and 8 others (2014) Retreat of Pine Island Glacier controlled by marine ice-sheet instability. *Nature Climate Change* **4**(2), 117–121. doi: 10.1038/nclimate2094.

Felikson D and 10 others (2025) Progress and future directions in constraining uncertainties in sea-level projections using observations. *Nature Climate Change* **15**, 1–13. doi: 10.1038/s41558-025-02437-4

Fowler A (1997) *Mathematical Models in the Applied Sciences*. Cambridge University Press.

Goldberg D, Gourmelen N, Kimura S, Millan R and Snow K (2019) How accurately should we model ice shelf melt rates?. *Geophysical Research Letters* **46**(1), 189–199.

Greene CA, Gardner AS, Schlegel NJ and Fraser AD (2022) Antarctic calving loss rivals ice-shelf thinning. *Nature* **609**(7929), 948–953. doi: 10.1038/s41586-022-05037-w.

Haseloff M and Sergienko OV (2018) The effect of buttressing on grounding line dynamics. *Journal of Glaciology* **64**(245), 417–431. doi: 10.1017/jog.2018.30.

Haseloff M and Sergienko OV (2022) Effects of calving and submarine melting on steady states and stability of buttressed marine ice sheets. *Journal of Glaciology* **68**(272), 1149–1166. doi: 10.1017/jog.2022.29.

Hewitt IJ (2020) Subglacial plumes. *Annual Review of Fluid Mechanics* **52**, 145–169. doi: 10.1146/annurev-fluid-010719-060252.

Hindmarsh RC (2012) An observationally validated theory of viscous flow dynamics at the ice-shelf calving front. *Journal of Glaciology* **58**(208), 375–387. doi: 10.3189/2012JoG11J206.

Holland PR, Feltham DL and Jenkins A (2007) Ice Shelf Water plume flow beneath Filchner-Ronne Ice Shelf, Antarctica. *Journal of Geophysical Research: Oceans* **112**(C05), 044. doi: 10.1029/2006JC003915.

Jenkins A (1991) A one-dimensional model of ice shelf-ocean interaction. *Journal of Geophysical Research: Oceans* **96**(C11), 20671–20677. doi: 10.1029/91JC01842.

Jenkins A (2011) Convection-driven melting near the grounding lines of ice shelves and tidewater glaciers. *Journal of Physical Oceanography* **41**(12), 2279–2294. doi: 10.1175/JPO-D-11-03.1.

Jordan JR, Miles BWJ, Gudmundsson GH, Jamieson SSR, Jenkins A and Stokes CR (2023) Increased warm water intrusions could cause mass loss in East Antarctica during the next 200 years. *Nature Communications* **14**(1), 1825. doi: 10.1038/s41467-023-37553-2.

Joughin I, Alley RB and Holland DM (2012) Ice-sheet response to oceanic forcing. *Science* **338**(6111), 1172–1176. doi: 10.1126/science.1226481.

Lambert E, Jüling A, van de Wal RSW and Holland PR (2023) Modelling Antarctic ice shelf basal melt patterns using the one-layer Antarctic model for dynamical downscaling of ice–ocean exchanges (LADDIE v1.0). *The Cryosphere* **17**(8), 3203–3228. doi: 10.5194/tc-17-3203-2023.

Lazeroms WMJ, Jenkins A, Gudmundsson GH and van de Wal RSW (2018) Modelling present-day basal melt rates for Antarctic ice shelves using a parametrization of buoyant meltwater plumes. *The Cryosphere* **12**(1), 49–70. doi: 10.5194/tc-12-49-2018.

Lazeroms WMJ, Jenkins A, Rienstra SW and Van De Wal RSW (2019) An analytical derivation of ice-shelf basal melt based on the dynamics of meltwater plumes. *Journal of Physical Oceanography* **49**(4), 917–939. doi: 10.1175/JPO-D-18-0131.1.

Levermann A and 36 others (2020) Projecting Antarctica's contribution to future sea level rise from basal ice shelf melt using linear response functions of 16 ice sheet models (LARMIP-2). *Earth System Dynamics* **11**(1), 35–76. doi: 10.5194/esd-11-35-2020.

MacAyeal DR (1985) Evolution of tidally triggered meltwater plumes below ice shelves. *Oceanology of the Antarctic Continental Shelf* **43**, 133–143.

MacAyeal DR (1989) Large-scale ice flow over a viscous basal sediment: Theory and application to ice stream B, Antarctica. *Journal of Geophysical Research: Solid Earth* **94**(B4), 4071–4087. doi: 10.1029/JB094iB04p04071.

Nick F, van der Veen C, Vieli A and Benn D (2010) A physically based calving model applied to marine outlet glaciers and implications for the glacier dynamics. *Journal of Glaciology* **56**(199), 781–794. doi: 10.3189/002214310794457344.

Nick FM, Vieli A, Howat IM and Joughin I (2009) Large-scale changes in Greenland outlet glacier dynamics triggered at the terminus. *Nature Geoscience* **2**(2), 110–114. doi: 10.1038/ngeo394.

Payne AJ, Holland PR, Shepherd AP, Rutt IC, Jenkins A and Joughin I (2007) Numerical modeling of ocean-ice interactions under Pine Island Bay's ice shelf. *Journal of Geophysical Research: Oceans* **112**(C10), 019. doi: 10.1029/2006JC003733.

Pegler SS (2016) The dynamics of confined extensional flows. *Journal of Fluid Mechanics* **804**, 24–57. doi: 10.1017/jfm.2016.516.

Pritchard HD and 10 others (2025) Bedmap3 updated ice bed, surface and thickness gridded datasets for Antarctica. *Scientific data* **12**(1), 414.

QGIS Development Team (2025) *QGIS Geographic Information System*. QGIS Association.

Reagan JR and 11 others (2024) *World Ocean Atlas 2023.*, Dataset: NCEI Accession 0270533.

Reese R, Albrecht T, Mengel M, Asay-Davis X and Winkelmann R (2018) Antarctic sub-shelf melt rates via PICO. *The Cryosphere* **12**(6), 1969–1985. doi: 10.5194/tc-12-1969-2018.

Rignot E, Jacobs S, Mouginot J and Scheuchl B (2013) Ice-shelf melting around Antarctica. *Science* **341**(6143), 266–270. doi: 10.1126/science.1235798.

Schoof C (2007) Marine ice-sheet dynamics. Part 1. The case of rapid sliding. *Journal of Fluid Mechanics* **573**, 27–55. doi: 10.1017/S0022112006003570.

Sergienko OV, Goldberg DN and Little CM (2013) Alternative ice shelf equilibria determined by ocean environment. *Journal of Geophysical Research: Earth Surface* **118**(2), 970–981. doi: 10.1002/jgrf.20054.

Seroussi H and 46 others (2020) ISMIP6 Antarctica: A multi-model ensemble of the Antarctic ice sheet evolution over the 21st century. *The Cryosphere* **14**(9), 3033–3070. doi: 10.5194/tc-14-3033-2020.

Straneo F and Heimbach P (2013) North Atlantic warming and the retreat of Greenland's outlet glaciers. *Nature* **504**(7478), 36–43.

van der Veen CJ (1998) Fracture mechanics approach to penetration of surface crevasses on glaciers. *Cold Regions Science and Technology* **27**(1), 31–47.

Virtanen P and 111 others (2020) SciPy 1.0: Fundamental algorithms for scientific computing in Python. *Nature Methods* **17**(3), 261–272. doi: 10.1038/s41592-019-0686-2.

Downloaded from https://www.cambridge.org/core. 14 Nov 2026 at 21:14:43, subject to the Cambridge Core terms of use.

Appendix A

Table A1. Parameters from the shallow shelf model and the plume models as described in the text.

Common			
Description	Variable	Value	Units
Gravity constant	g	9.81	$m\,s^{-2}$
Seawater density	ρ_w	1000	$kg\,m^{-3}$
Ice density	ρ_i	900	$kg\,m^{-3}$
Rate factor	A	10^{-24}	$Pa^{-3}\,s^{-1}$
Flow law exponent	n	3	—

Table A2. Parameters and variables of the plume models as described in the text. Following Jenkins (2011), we replace T_f with T_{af} in the expressions of M_0 and T_i^{ef} in our simulations, which simplifies the numerical integration and has no measurable impact on the results.

Plume			
Description	Variable	Value	Units
Haline contraction coefficient	β_S	7.86×10^{-4}	1
Thermal expansion coefficient	β_T	3.87×10^{-5}	K^{-1}
Specific heat capacity of seawater	c	3.974×10^{3}	$J\,kg^{-1}\,K^{-1}$
Specific heat capacity of ice	c_i	2.009×10^{3}	$J\,kg^{-1}\,K^{-1}$
	c_{ρ_1}	$L\beta_T/(\Gamma\beta_S S_a c)$	—
	c_{ρ_2}	$-\lambda_1\beta_T/\beta_S$	—
	c_τ	c_{ρ_2}/c_{ρ_1}	—
Slope correction parameter	C_ϵ	0.6	—
Lateral shear stress parameter	C_W	$2\,(n+1)^{\frac{1}{n}}$	—
Drag coefficient	C_d	2.5×10^{-3}	—
Ambient density contrast slope	$\frac{d\Delta\rho_a}{dz_b}$	$\beta_S\frac{dS_a}{dz_b} - \beta_T\frac{dT_a}{dz_b}$	m^{-1}
Effective melt-water density contrast	$\Delta\rho_i^{ef}$	$\beta_S\,(S_a - S_i) - \beta_T\left(T_a - T_i^{ef}\right)$	—
Entrainment coefficient	E_0	3.6×10^{-2}	—
Effective thermal Stanton number	Γ	5.9×10^{-4}	—
Latent heat of fusion for water	L	3.35×10^{5}	$J\,kg^{-1}$
Seawater freezing point slope	λ_1	-5.73×10^{-2}	°C
Seawater freezing point offset	λ_2	8.32×10^{-2}	°C
Depth dependence of freezing point	λ_3	7.61×10^{-4}	$°C\,m^{-1}$
Basal slope	$\sin\alpha$	$-\partial h/\partial x/\sqrt{\rho_w^2/\rho_i^2 + \lvert\partial h/\partial x\rvert^2}$	—
Melt rate factor	M_0	$\Gamma/\left(T_f - T_i^{ef}\right)$	$°C^{-1}$
Ice salinity	S_i	0	psu
Ice temperature	T_i	0	°C
Plume freezing temperature	T_f	$\lambda_1 S + \lambda_2 + \lambda_3 z_b$	°C
Ambient freezing temperature	T_{af}	$\lambda_1 S_a + \lambda_2 + \lambda_3 z_b$	°C
Effective meltwater temperature	T_i^{ef}	$T_f - L/c - c_i(T_f - T_i)/c$	°C
Meltwater freezing temperature	T_{if}	$\lambda_1 S_i + \lambda_2 + \lambda_3 z_b$	°C

Downloaded from https://www.cambridge.org/core. 14 Nov 2026 at 21:14:43, subject to the Cambridge Core terms of use.

Appendix B

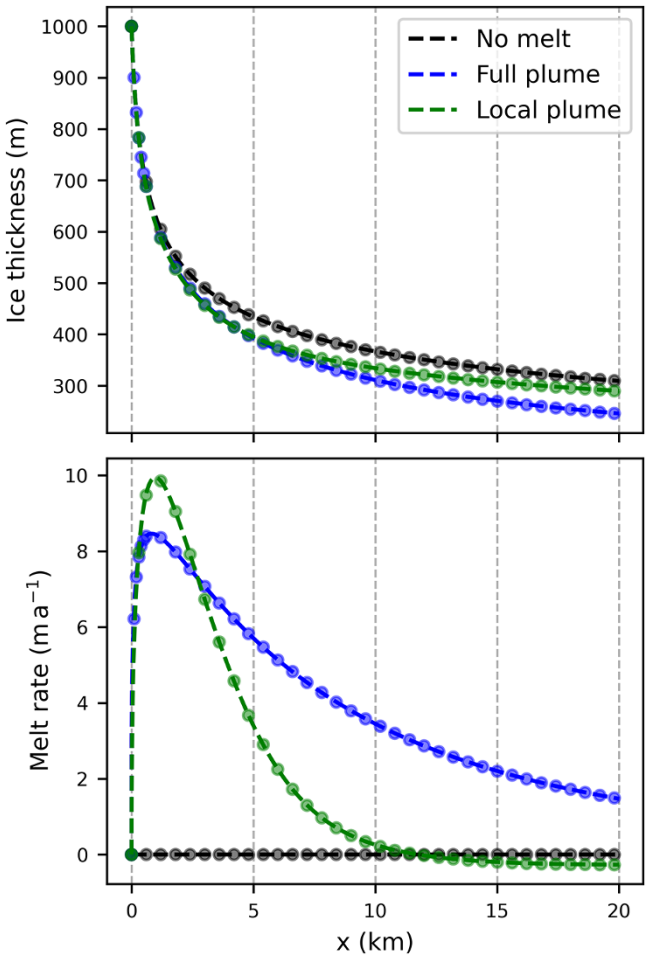


Figure B1. Steady-state ice profiles (top) and melt rates (bottom) calculated using Python (dashed lines) and PETSc (dots) for ambient ocean temperature $T_a = -1.9°C$. Three different melt parameterizations are shown: no melt (black), the local plume model (green) and the full plume model (blue).

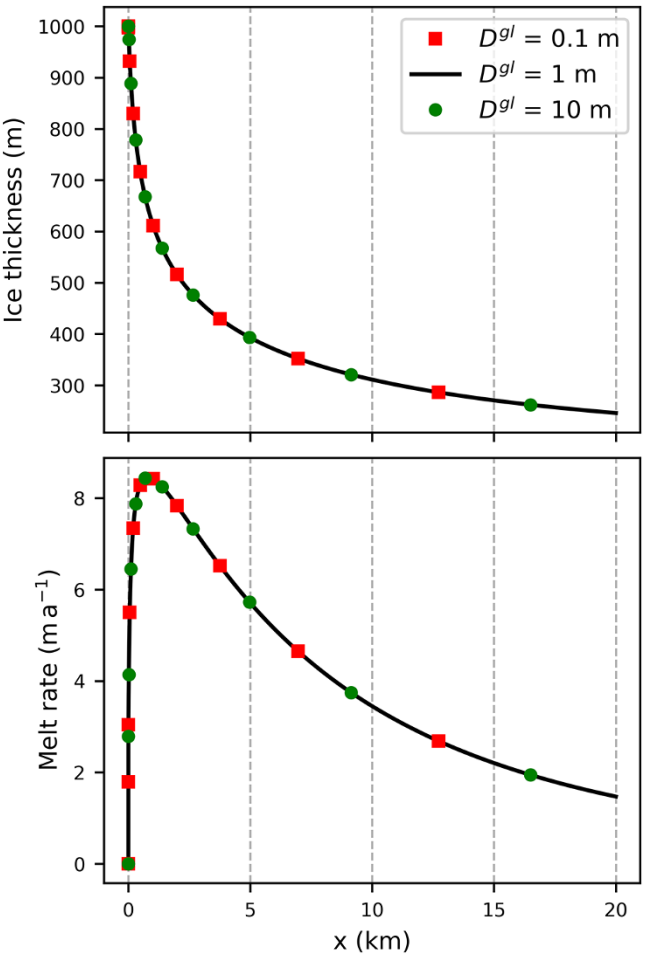


Figure B2. Influence of the initial plume thickness D^{gl} on the coupled system with the full plume model: $D^{gl} = 0.1$ m (red), $D^{gl} = 1$ m (black) and $D^{gl} = 10$ m (green). The ambient ocean temperature is $T_a = -1.9°C$. Note that the results are not sensitive to a change in D^{gl} across three orders of magnitude.

Downloaded from https://www.cambridge.org/core. 14 Nov 2026 at 21:14:43, subject to the Cambridge Core terms of use.

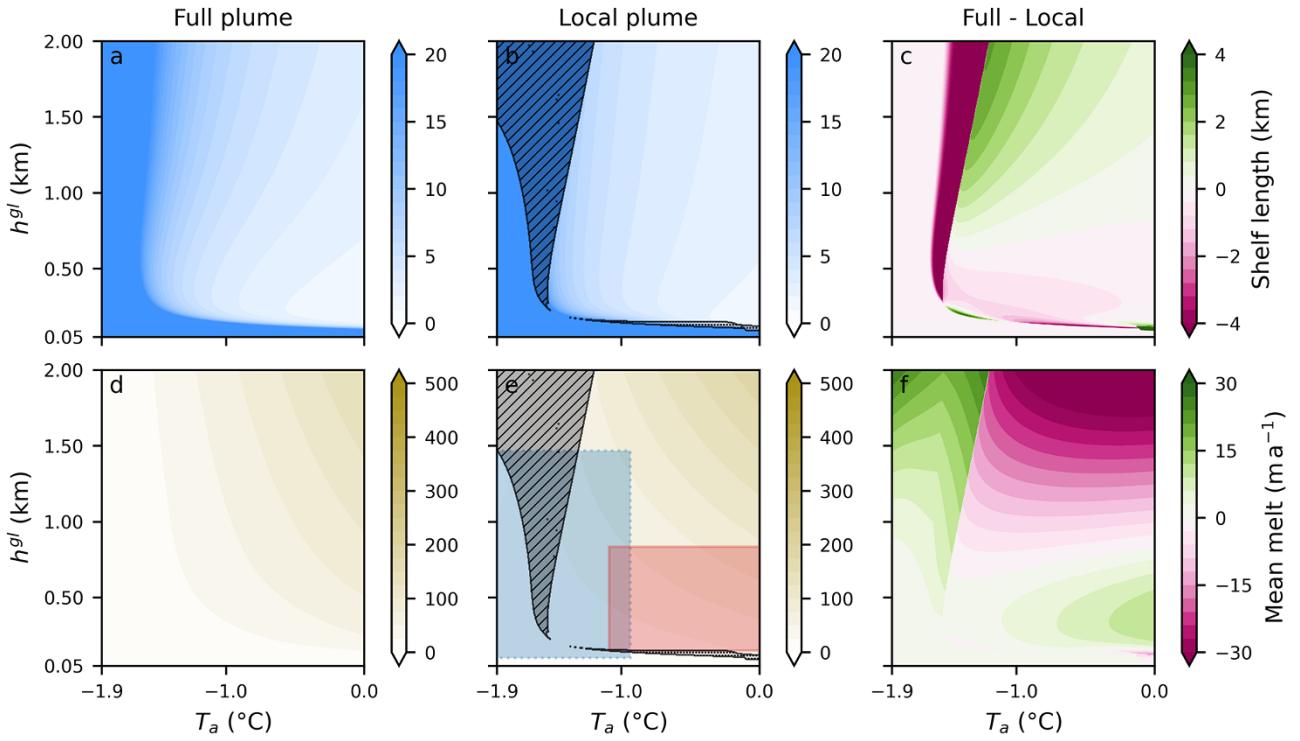


Figure B3. Identical to Figure 5 but with the plume parameterization from Lazeroms and others (2018) instead of that from Lazeroms and others (2019).

Appendix C

We selected 18 ice shelves to broadly represent the conditions at the base of Antarctic ice shelves. The selection was made to ensure a geographically representative distribution around Antarctica while focusing on the larger ice shelves. The two boxes shown in Fig. 5 were derived using QGIS (QGIS Development Team, 2025) as described below.

Ocean temperatures were obtained from the World Ocean Atlas 2023 dataset for both winter and summer (Reagan and others, 2024), with one exception for Pine Island, where we used the ocean temperature data from Burgard and others (2022) since the World Ocean Atlas 2023 missed data. Each ice shelf was manually delineated, with the masking region extending a few grid cells in front of the shelves. The temperature was averaged both spatially across each shelf from the sea bed to 200 m below sea level, and temporally across summer and winter. The 200 m depth temperature was selected as a representative proxy for potential warm water intrusions into the ice shelf cavities. The separation of shelves into two groups was solely based on the temperature because it creates a clear distinction with a threshold at -1°C. The 'cold' regime comprises the Ross, Mertz, Totten, Shackleton, Amery, Filchner, Ronne, Larsen and Dotson ice shelves (blue box, $T_a = [-1.9, -0.9]$°C). These shelves are located farther south and further from the continental shelf edge than other ice shelves, thereby remaining isolated from the Antarctic Circumpolar Current. In contrast, the 'warm' regime includes the Rennick, Cook, Baudouin, Stancomb-Brunt, Wilkins, Abbot, Getz, Pine Island and Fimbul ice shelves (red box, $T_a = [-1.1, 0.5]$°C), which are closer to the continental shelf break, more exposed to warmer water and subject to higher levels of basal melting.

The grounding line position and ice thickness were obtained from Bedmap3 (Pritchard and others, 2025). To account for uncertainties related to grounding zone migration, the entire grounding line was buffered by 2 km. For each ice shelf, the grounding line was segmented into distinct polygons. Ice thickness statistics were derived for each grounding zone polygon separately (grouped by ice shelf), excluding grid points with zero ice thickness. Finally, the boundaries of each box in Fig. 5 are defined as the extrema of the mean $\pm$ one standard deviation for each ice shelf.

The 'realistic' temperature profile used in Fig. 2 is extracted from Burgard and others (2022). It represents a simulated mean temperature profile averaged in front of Thwaites Ice Shelf. The simulation was performed with NEMO (Nucleus for European Modelling of the Ocean) under realistic conditions as defined in Burgard and others (2022).

Downloaded from https://www.cambridge.org/core. 14 Nov 2026 at 21:14:43, subject to the Cambridge Core terms of use.